Research Paper

What kinds of urban forms can balance solar radiation and heat risk

A spatial analysis framework for climate-resilient cities

Yifan GUO, Southeast University, China

Abstract

Solar radiation is the foundation of the Earth's environmental evolution, which has enormous potential for utilization. However, excessive accumulation of solar radiation in high-density urban areas may also increase heat risks, especially when extreme heat events have become increasingly frequent in recent years. As solar radiation has both positive and negative effects on cities, it is crucial to explore spatial planning strategies that balance solar radiation utilization and heat risk resistance. Solving this problem is important for improving urban energy sustainability and climate resilience under extreme weather conditions. This study focuses on what kinds of urban forms can balance solar radiation and heat risk, so as to better adapt to extreme weather conditions, particularly heatwaves and long periods of high temperatures. This process is achieved by the spatial mapping and overlaying of multi-source data based on GIS analysis. Remote sensing data is corrected and downscaled to form a high-resolution urban dataset for mapping the distribution of solar radiation and heat risk in detail. The metrics for solar radiation potential and thermal risk are calculated using remote sensing data, comprehensively evaluating solar radiation capture and heat accumulation. The relationship of the parameters is explored using machine learning methods, providing quantitative evidence for the formulation of climate resilience-oriented strategies. The main contribution of this study is the development of a new framework for coupling solar radiation and heat risk, which offers a solid foundation for climate-resilient planning and policy-making. By comparing the results of different parts of the city, key areas that need to focus on cooling or solar radiation use are identified. The high resolution and spatial positioning of the research method enable it to guide precise interventions of planning strategies, such as urban form adjustment, photovoltaic utilization, and green infrastructure development. Additionally, this framework also makes it possible for planners to predict the solar potential and thermal risk resilience of schemes during the preliminary design stage. By adjusting urban form parameters in the digital model, the prediction results can be quickly generated. This allows planners to apply approaches that are better suited to the specific scenarios, thereby assisting urban design guidelines, key area renovations, and other initiatives.

Keywords

Urban form, Solar radiation, Heat risk

1. Introduction

The sun is the fundamental source of energy for the Earth (Wu *et al.*, 2024; Rostami and Nasrollahi, 2025). As the most abundant and sustainable renewable energy source, solar energy has drawn increasing global attention due to its potential to alleviate the energy crisis and reduce greenhouse gas emissions. According to the GLOBAL STATUS REPORT 2025, global solar photovoltaic generation continues to increase rapidly, highlighting the growing role of solar energy in carbon neutrality and energy transition.

However, the other side of solar radiation is its intensifying impact on the overheating of cities. With urban expansion, impermeable surfaces and dense building structures replace natural vegetation, altering the energy balance on the ground surface (Chakraborty and Qian, 2024; Hou *et al.*, 2025). These surfaces reduce albedo and lock in heat, resulting in an increase in surface heat storage and a decrease in heat dissipation capacity. Urban expansion and dense built environments intensify heat accumulation and reduce heat dissipation, contributing to increasing urban thermal risks under global warming (Ouyang *et al.*, 2022; Perkins-Kirkpatrick *et al.*, 2024).

A large number of studies have warned that urban form is closely related to heat risk, revealing the correlation between building density, layout, and the increase in surface temperature, urban heat island, and heat exposure (Huang and Wang, 2019; Li *et al.*, 2021; Ming *et al.*, 2023). A study of 31 cities in China shows that during the period from 2000 to 2020, the daytime heat island effect increased in over 80% of the cities, with urban expansion and vegetation reduction being the main factors (Yu *et al.*, 2025). With the expansion of urban space, the impact of urban areas on surface temperature is also increasing. Reasonable planning of urban land is of great significance for alleviating the heat island effect (Guo *et al.*, 2020). Meanwhile, the urban form will also affect the acquisition of solar radiation by changing the shading relationship, the material of the underlying surface, the degree of solar trap, and thereby influence the utilization potential of renewable energy (Kaleshwarwar and Bahadure, 2023; Yang *et al.*, 2023) and energy balance (Yang *et al.*, 2023).

Although there have been abundant research achievements on the urban heat island effect, thermal comfort and microclimate regulation, the research on solar radiation itself, which traces these phenomena back to the fundamental energy driving source, is relatively scarce. Furthermore, studies often regard solar energy utilization and urban heat mitigation as independent topics. This fragmentation leaves the core issue unresolved: What kinds of urban forms can simultaneously reduce thermal risks and enhance the utilization rate of solar energy? Answering this question is crucial for shaping future urban spatial planning, which requires efficient utilization of solar energy while minimizing thermal risks as much as possible under the long-term issue of climate change.

To bridge this gap, this study develops a spatial coupling framework linking solar radiation potential and thermal risk to identify urban morphology patterns that support both renewable energy utilization and climate resilience. The framework can support planning decisions related to photovoltaic deployment, shading strategies, and green infrastructure.

2. Methodology

2.1. Study area

Jiangsu Province, located in eastern China within the Yangtze River Delta, was selected as the study area due to its high urbanization level, dense built environment, rapid photovoltaic development, and

increasing frequency of extreme heat events (Figure 1). The province covers approximately 107,200 km^2 and contains 13 major cities with strong spatial heterogeneity in urban morphology. In recent years, Jiangsu has actively promoted renewable energy development, while also experiencing intensified summer heat waves, making it an appropriate case for examining the balance between solar energy utilization and thermal risk mitigation.

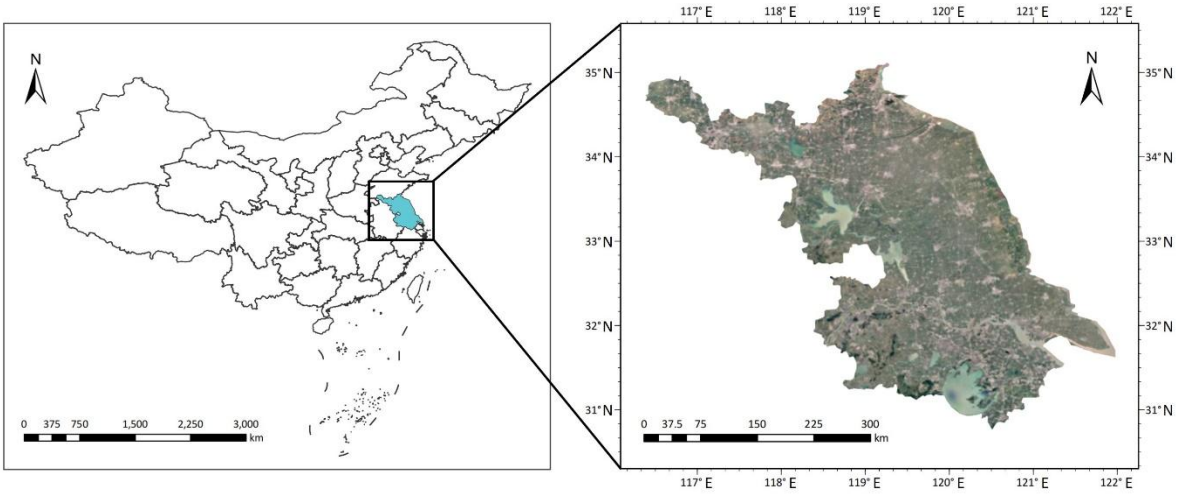


Figure 1. Research Area, Jiangsu Province, China. Source: Author's own elaboration based on base map data from National Platform for Common GeoSpatial Information Services (Tianditu) and satellite imagery from Google Earth.

2.2. Multi-source data acquisition

The main methods adopted in this paper include multi-source data overlay and statistical analysis. The workflow is shown in Figure 2. The data involved in this study were obtained from open-source datasets. Solar radiation data were obtained from the NSRDB dataset, using summer (June to August 2020) global horizontal irradiance (GHI) (Sengupta et al., 2018). Land surface temperature (LST) data were obtained from the National Science Data Center for the Tibetan Plateau (Zhou et al., 2017; Zhang et al., 2019, 2021). LST data were used as indicators of thermal risk due to their ability to reflect surface thermal conditions with high spatiotemporal accuracy.

Urban morphology data were derived from a 100-meter resolution Local Climate Zone (LCZ) map (Demuzere *et al.*, 2022), with the calculation methodology detailed in Section 2.3. The LCZ map divides the urban surface into 17 categories based on LCZ typology, explaining its micro-scale land cover and related physical characteristics. Among them, 10 types are built environments and 7 are natural environments (Stewart and Oke, 2012).

Data above were preprocessed in ArcGIS Pro. Firstly, the data within the research scope of Jiangsu Province was obtained through Mask extraction. Then, use the majority filter method to complete the default values. Finally, for the data with inconsistent resolutions, integration is carried out. Considering the data accuracy, computing speed, and the guiding significance of the analysis results for urban planning comprehensively, a grid with a resolution of 1km is selected to unify the multi-source data. For data with an accuracy of less than 1km, bilinear interpolation is used for resampling. Finally, the integrated raster data of solar radiation, land surface temperature, and urban morphology in Jiangsu Province were obtained.

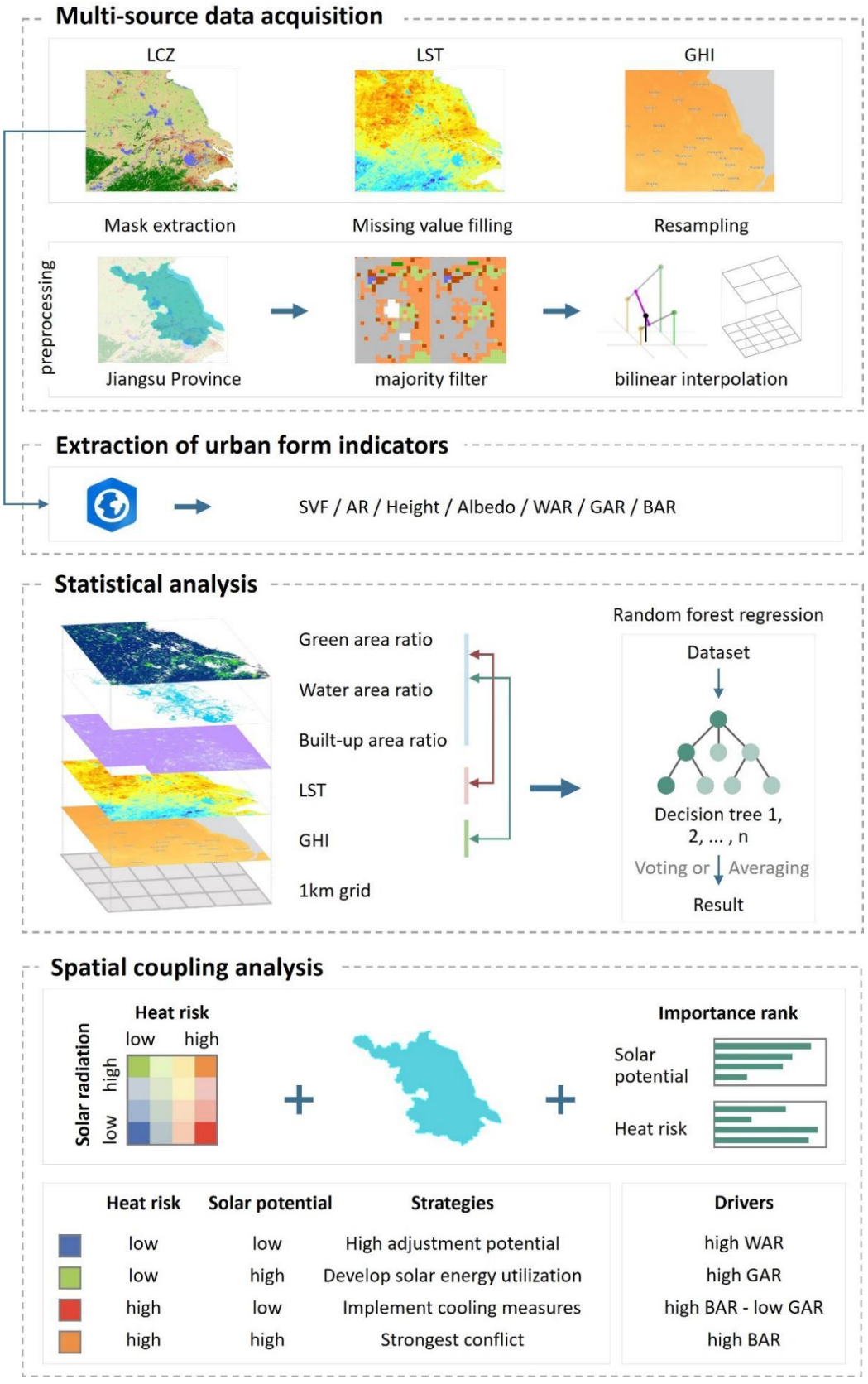

Multi-source data acquisition
LCZ
LST
GHI
Mask extraction
Missing value filling
Resampling
preprocessing
Jiangsu Province
majority filter
bilinear interpolation
Extraction of urban form indicators
SVF / AR / Height / Albedo / WAR / GAR / BAR
Statistical analysis
Green area ratio
Water area ratio
Built-up area ratio
LST
GHI
1km grid
Random forest regression
Dataset
Decision tree 1, 2, ... , n
Voting or Averaging
Result
Spatial coupling analysis
Heat risk
low
high
Solar radiation
high
low
Importance rank
Solar potential
Heat risk
Heat risk
Solar potential
Strategies
Drivers
low
low
High adjustment potential
high WAR
low
high
Develop solar energy utilization
high GAR
high
low
Implement cooling measures
high BAR - low GAR
high
high
Strongest conflict
high BAR

Figure 2. Workflow of the research. Source: Author's own elaboration based on solar radiation data from NSRDB, land surface temperature data from the National Science Data Center for the Tibetan Plateau, and LCZ data from Demuzere et al., 2022.

2.3. Extraction of urban form indicators

Since LCZ covers different types of built and natural environments, and each type has a corresponding range of indicators (Table 1), the urban morphological indicators within a certain range can be calculated based on the high-precision LCZ map.

LCZ	Description	BSF	PSF	SVF	AR	Height	Albedo
1	Compact high-rise	40-60 (50)*	<10 (5)	0.2-0.4 (0.3)	>2 (2.5)**	>25 (40)	0.10-0.20 (0.15)
2	Compact midrise	40-70 (55)	<20 (10)	0.3-0.6 (0.45)	0.75-2 (1.375)	10-25 (17.5)	0.10-0.20 (0.15)
3	Compact low-rise	40-70 (55)	<30 (15)	0.2-0.6 (0.4)	0.75-1.5 (1.125)	3-10 (6.5)	0.10-0.20 (0.15)
4	Open high-rise	20-40 (30)	30-40 (35)	0.5-0.7 (0.6)	0.75-1.25 (1)	>25 (35)	0.12-0.25 (0.185)
5	Open midrise	20-40 (30)	20-40 (30)	0.5-0.8 (0.65)	0.3-0.75 (0.525)	10-25 (17.5)	0.12-0.25 (0.185)
6	Open low-rise	20-40 (30)	30-60 (45)	0.6-0.9 (0.75)	0.3-0.75 (0.525)	3-10 (6.5)	0.12-0.25 (0.185)
7	Lightweigh t low-rise	60-90 (75)	<30 (15)	0.2-0.5 (0.35)	1-2 (1.5)	2-4 (3)	0.15-0.35 (0.25)
8	Large low-rise	30-50 (40)	<20 (10)	>0.7 (0.85)	0.1-0.3 (0.2)	3-10 (6.5)	0.15-0.25 (0.2)
9	Sparsely built	10-20 (15)	60-80 (70)	>0.8 (0.9)	0.1-0.25 (0.175)	3-10 (6.5)	0.12-0.25 (0.185)
10	Heavy industry	20-30 (25)	40-50 (45)	0.6-0.9 (0.75)	0.2-0.5 (0.35)	5-15 (10)	0.12-0.20 (0.16)
A	Dense trees	<10 (5)	>90 (95)	<0.4 (0.2)	>1 (1.5)	3-30 (16.5)	0.10-0.20 (0.15)
B	Scattered trees	<10 (5)	>90 (95)	0.5-0.8 (0.65)	0.25-0.75 (0.5)	3-15 (9)	0.15-0.25 (0.2)
C	Bush, scrub	<10 (5)	>90 (95)	0.7-0.9 (0.8)	0.25-1.0 (0.625)	<2 (1)	0.15-0.30 (0.225)
D	Low plants	<10 (5)	>90 (95)	>0.9 (0.95)	<0.1 (0.05)	<1 (0.5)	0.15-0.25 (0.2)
E	Bare rock or paved	<10 (5)	<10 (5)	>0.9 (0.95)	<0.1 (0.05)	<0.25 (0.125)	0.15-0.30 (0.225)
F	Bare soil or sand	<10 (5)	>90 (95)	>0.9 (0.95)	<0.1 (0.05)	<0.25 (0.125)	0.20-0.35 (0.275)

G	Water	<10 (5)	>90 (95)	>0.9 (0.95)	<0.1 (0.05)	(0)	0.02-0.10 (0.06)

Table 1. LCZ type and range of related indicators.

*** The value in parentheses is the median used in calculations.**

**** For ranges not specified, common values from relevant studies are referenced.**

This paper extracts seven indicators from the 100m-resolution LCZ map: Sky View Factor (SVF), Aspect Ratio (AR), Height, Albedo, Green Area Ratio (GAR), Water Area Ratio (WAR), and Built-up Area Ratio (BAR). These metrics are frequently employed in urban environmental research and can, to some extent, reflect urban morphology (Hasan and Horvat, 2023; Liu *et al.*, 2024). At the 1km grid level, each grid contains 10×10 LCZ grid data points. First, the proportion p_i of each LCZ type is calculated. The proportion of LCZ G is treated as WAR. BAR is computed as the weighted average of the Building Surface Fraction (BSF) corresponding to each LCZ type, where BSF data uses the median value within the range. GAR is calculated as the Pervious Surface Fraction (PSF) excluding bare and water areas, since PSF includes both vegetation, bare soil, and water surfaces. The formula is as follows:

$$\text{Water area ratio} = \frac{\text{Area (LCZ G)}}{\text{Area (total)}}$$

$$\text{Green area ratio} = \sum (\text{PSF}_i \cdot p_i),\ i \in [1, 15]$$

$$\text{Built-up area ratio} = \sum (\text{BSF}_i \cdot p_i)$$

2.4. Calculation of Thermal Risk and Solar Radiation Indicators

To identify the impact of urban form on surface temperature and solar radiation, this study conducted a statistical analysis on acquired data. First, based on preprocessed raster data, the following pixel-level metrics were calculated: (i) average thermal conditions, namely the summer daytime and nighttime LST mean; (ii) extreme heat indicators, using the 90th percentile LST, a common metric in urban climate and thermal environment research (Tavakol, Rahmani and Harrington, 2020), to reflect temperature levels during the hottest 10% of days. Specifically, for each pixel, LST values during June to August were extracted, and the 90th percentile (P90) was computed from the temporal distribution. Daytime and nighttime values were calculated separately based on satellite overpass time; (iii) the relative solar radiation potential under clear conditions, represented by the Z-score of the 90th percentile GHI. The Z-score was calculated as:

$$Z = \frac{GHI_{P90,\,i} - \mu}{\sigma}$$

Where $GHI_{P90,\,i}$ is the 90th percentile GHI of pixel i, and μ and σ are the mean and standard deviation of all pixels.

The P90 effectively filters out large-scale disturbances such as cloud cover, weather events, and seasonal variations. Further standardizing the P90 values with Z-scores positions the pixel's radiation potential relative to the overall distribution within the study area, unaffected by absolute radiation levels, latitude gradients, or cloud frequency differences. This enables comparisons of radiation potential across different spatial units within the city.

2.5. Statistical Modelling and Spatial Coupling Analysis

Based on the derived indicators, statistical modelling and spatial coupling analysis were conducted. All urban morphology indicators were treated as independent variables, while LST and GHI metrics were used as dependent variables. Subsequently, random forest regression was applied to each indicator against urban form to assess influence levels. SHAP was employed to interpret variable weights.

By spatially overlaying solar radiation potential with extreme heat indicators, four categories of areas are identified: (i) High potential-high risk areas, where thermal risk conflicts most intensely with solar energy utilization potential. (ii) High potential-low risk areas, suitable for solar energy development. (iii) Low potential-high risk areas, requiring prioritized cooling measures. (iv) Low potential-low risk areas, where planning adjustments can be made based on specific needs. Heat maps were used to visualize the distribution of these areas. Single-factor analysis of variance (ANOVA) was conducted on the urban forms of each category to assess differences in their urban form patterns, thereby supporting planning decisions.

3. Results

3.1. Regression results

This study systematically analyzed the influence mechanisms of seven urban morphological factors on five thermal and solar environment indicators using a random forest regression model combined with SHAP interpretation. The results demonstrate consistent patterns in relative importance across daytime and nighttime thermal environments as well as solar radiation responses. Among all factors, WAR, BAR, building height, and albedo consistently showed higher importance across most models. For example, in thermal indicators such as daytime LST mean, daytime LST P90, and nighttime LST P90, the importance of WAR and BAR remained stable at approximately 17% to 19%. Building height and albedo made the largest contributions in models for daytime LST mean, nighttime LST P90, and GHI, with values reaching up to 19.5%.

The SHAP analysis further clarifies the directional effects of these variables (Figure 3). WAR generally shows a clear negative contribution, indicating its effectiveness in reducing both daytime and nighttime temperatures. BAR and height exhibit consistent positive effects, supporting their roles in temperature intensification as shown in the SHAP results. In contrast, although SVF and AR demonstrate relatively lower importance, SHAP outputs suggest that their effects are more condition-dependent across temporal scales, reflecting the complexity of morphological control on radiative transfer. Overall, the random forest importance ranking offers a quantitative assessment of factor influence, while the SHAP interpretation provides insight into the contribution direction and behavioral sensitivity of each factor across different value ranges.

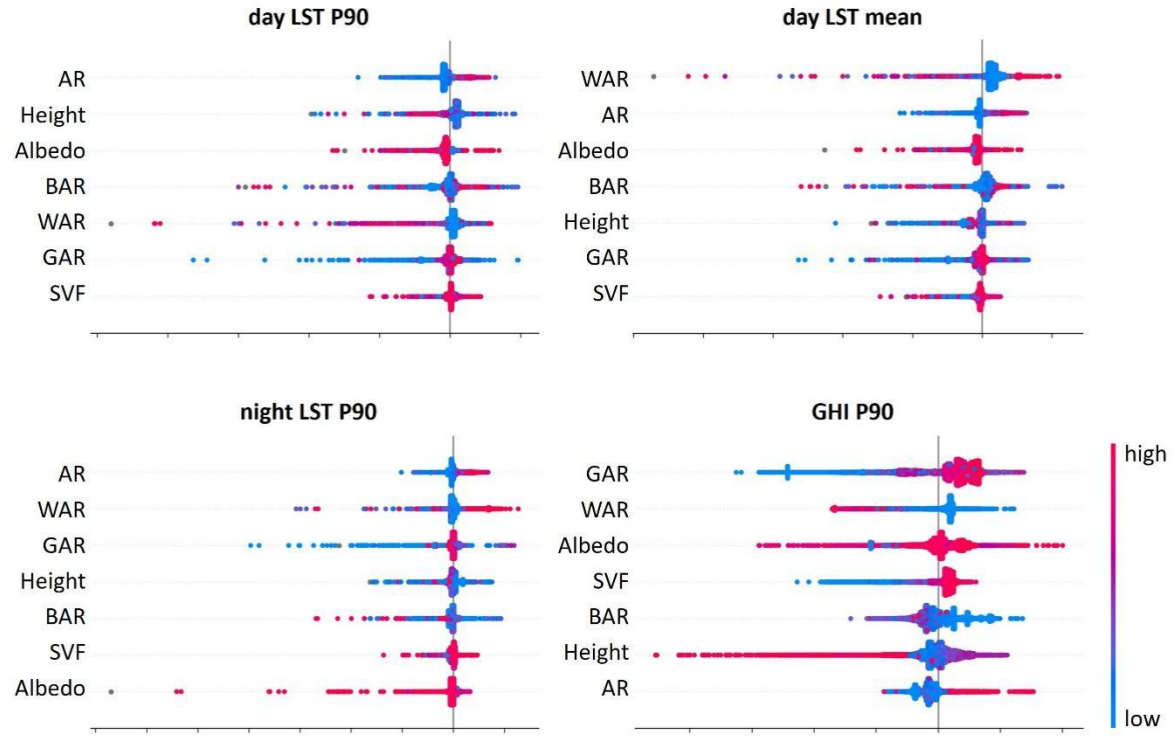


Figure 3. SHAP plot of 7 urban morphology indicators. Source: Author's own elaboration using SHAP analysis in Python.

3.2. Results of spatial overlay analysis

The spatial overlay of solar radiation potential and extreme heat indices is shown in Figure 4(a). Four distinct regional categories exhibit clear distribution patterns. These categories were further isolated (Figure 4(c)) and spatially compared with the LCZ map (Figure 4(b)), which represents land cover information in Jiangsu Province. It is found that the L-L zone highly overlaps with the locations of rivers, lakes, and other water bodies. The L-H zone is almost entirely situated within the vegetation zones of LCZ A-D, while the H-L zone predominantly occurs in areas with concentrated built-up environments.

The results of the analysis of variance revealed significant differences in the urban morphological structure among different regions. The F values of BAR in the four typical regions were relatively high ($F=3993.91$, $p<0.0001$), indicating that these regions not only have obvious distinguishability in the proportion of built-up areas, but also show a high degree of consistency within each group. The BAR in the H-L region was significantly higher than that in other regions, indicating a strong correlation between the increase in the density of built areas and extremely high-temperature events. High-density urban areas also exhibit reduced solar radiation potential due to shading effects. Regarding GAR, analysis of variance also showed significant differences ($p<0.0001$), among which the values in the L-H region were significantly higher than those in other regions. Low-risk and high-potential areas are more common in vegetation-covered areas, and high-GAR areas generally have stronger solar radiation potential. The difference in the proportion of water bodies is relatively weak but still statistically significant. The L-L region is more closely associated with large water bodies. By comparing the BAR, SVF, AR and Height in the H-L and H-H regions, it can be concluded that under the same degree of thermal risk, the solar radiation potential in dense urban areas can be enhanced by appropriately reducing BAR, AR and Height and increasing SVF. This implies that in high-density urban areas, planning interventions such as reducing

excessive building compactness, optimizing height distribution, and increasing sky view factor through street layout design can improve solar access while maintaining acceptable thermal conditions. Overall, the statistical results are consistent with the spatial patterns of visual recognition in the bivariate map.

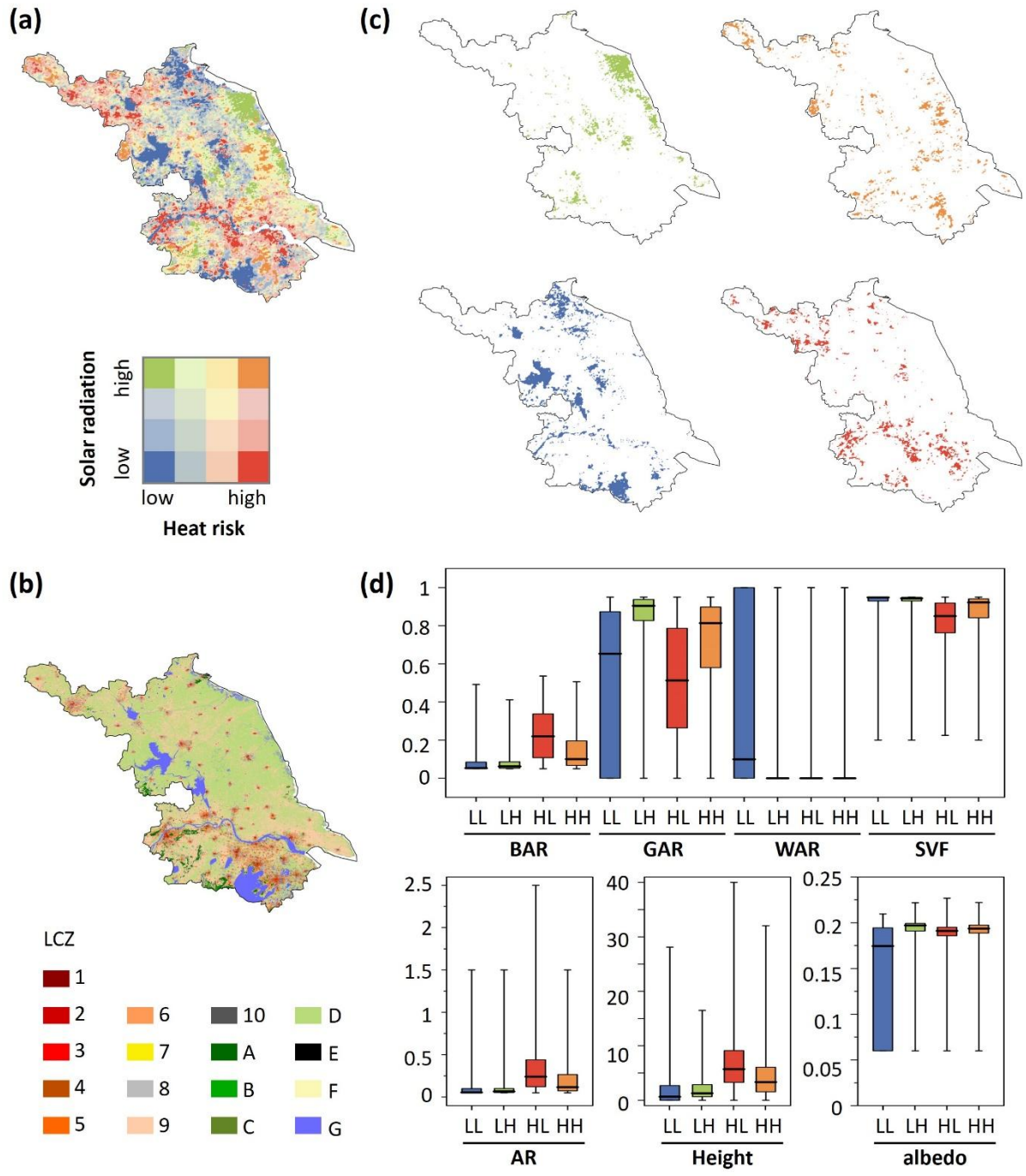


Figure 4. Result of spatial coupling analysis. (a) Heat risk-solar radiation dual-variable spatial coupling map. (b) LCZ map. (c) Four typical regions. (d) Results of single-factor ANOVA for BAR, GAR, WAR, SVF, AR, Height, and Albedo in four typical regions. Source: Author's own elaboration based on multi-source datasets (NSRDB, LST, and LCZ) and statistical analysis results.

The analysis suggests that regions with high solar potential and relatively low thermal risk generally exhibit BAR values between 6.24% and 10.02%, providing a potential reference range for planning and density control. In practical terms, this range can serve as a reference for zoning regulations or urban design guidelines, supporting the formulation of density control standards in areas aiming to achieve both high solar potential and manageable thermal risk.

In addition, as a region with poor thermal-radiation performance, the median of multiple indicators of H-L can be used as the early warning threshold for identifying potential risk areas. For instance, when the average height exceeds 5.71 meters, attention should be paid to the potential high heat risk and the possibility of low solar radiation utilization. However, these thresholds should be interpreted as empirical reference values rather than fixed standards.

4. Conclusion

This study developed a spatial coupling framework integrating solar radiation potential and thermal risk to explore how urban morphology influences energy utilization and heat exposure. Taking Jiangsu Province as an example, this framework combines multi-source remote sensing, machine learning analysis and spatial coupling to reveal how changes in surface properties, built environment and land cover jointly regulate radiation gain and heat accumulation. In urban climate and energy research, the perspectives of solar energy and heat are usually dealt with separately. By unifying these two perspectives, this study provides a more comprehensive understanding of how cities can balance the challenges of climate mitigation and adaptation.

The research results show that the potential of solar radiation and thermal risk form a highly structured spatial pattern, reflecting the composition of land cover and urban form. Areas dominated by water always correspond to regions with low radiation potential and low heat risk. The vegetation area shows a high potential for solar radiation while maintaining a relatively low temperature, while the compact built-up area exhibits strong heat accumulation and reduced radiation availability due to shading effects, rough surfaces and three-dimensional shapes. The four spatial classifications not only capture spatial differences, but also provide a practical basis for differentiating planning strategies in different urban contexts.

The random forest model and SHAP interpretation further reveal the multi-factor nature of the urban radiant thermal environment. Building height and albedo have a significant impact on surface temperature and solar radiation potential, with their importance percentages both exceeding 19%. Statistical verification using analysis of variance confirmed that there were significant differences among these four categories in all measured morphological parameters. This study identified the characteristic parameter range. For instance, maintaining BAR at approximately 6.24% to 10.02% tends to favor better light-thermal conditions. These ranges are not prescribed design standards but empirically derived reference values, reflecting the morphological trends of regions that exhibit high solar energy utilization potential and controllable thermal risks. Similarly, the values observed in the H-L region, such as higher building heights and BAR, can serve as early warning indicators of potential thermal radiation conflicts and provide information for risk-sensitive planning practices.

Overall, this study provides a generalizable methodological framework and a set of empirical insights that can support climate-resilient urban planning. In addition, this framework provides a foundation for scalable vertical applications. Future research can apply this approach to other regions, compare cross-city models, and combine time datasets to assess how continuous urban development reshapes the

radiation and thermal environment over time. As cities are confronted with ever-growing energy demands and increasingly severe extreme temperatures, it is becoming increasingly important to combine solar energy utilization strategies with thermal risk mitigation. The findings can support climate-sensitive planning strategies aimed at balancing renewable energy utilization and thermal risk mitigation.

5. References

REN21. 'GLOBAL STATUS REPORT 2025', REN21 [online]. Available at: https://www.ren21.net/gsr-2025/technologies/solar-pv/ (Accessed: 3 October 2025).

Carrington, D. (2025) 'World's major cities hit by 25% leap in extremely hot days since the 1990s', The Guardian, 30 September.

Chakraborty, T.C. and Qian, Y. (2024) "Urbanization exacerbates continental- to regional-scale warming," *ONE EARTH*, 7(8), pp. 1387–1401. Available at: https://doi.org/10.1016/j.oneear.2024.05.005.

Demuzere, M. *et al.* (2022) "A global map of local climate zones to support earth system modelling and urban-scale environmental science," *Earth System Science Data*, 14(8), pp. 3835–3873. Available at: https://doi.org/10.5194/essd-14-3835-2022.

Guo, A. *et al.* (2020) "Impact of urban morphology and landscape characteristics on spatiotemporal heterogeneity of land surface temperature," *Sustainable Cities and Society*, 63, p. 102443. Available at: https://doi.org/10.1016/j.scs.2020.102443.

Hasan, J. and Horvat, M. (2023) "Spatial parameters and methodological approaches in solar potential assessment - State-of-the-art," *Renewable and Sustainable Energy Reviews*, 188, p. 113857. Available at: https://doi.org/10.1016/j.rser.2023.113857.

Hou, Z. *et al.* (2025) "Radiative forcing reduced by early twenty-first century increase in land albedo," *Nature*, 641(8065), pp. 1162–1171. Available at: https://doi.org/10.1038/s41586-025-08987-z.

Huang, X. and Wang, Y. (2019) "Investigating the effects of 3D urban morphology on the surface urban heat island effect in urban functional zones by using high-resolution remote sensing data: A case study of Wuhan, Central China," *ISPRS Journal of Photogrammetry and Remote Sensing*, 152, pp. 119–131. Available at: https://doi.org/10.1016/j.isprsjprs.2019.04.010.

Kaleshwarwar, A. and Bahadure, S. (2023) "Assessment of the solar energy potential of diverse urban built forms in Nagpur, India," *Sustainable Cities and Society*, 96, p. 104681. Available at: https://doi.org/10.1016/j.scs.2023.104681.

Li, H. *et al.* (2021) "Quantifying 3D building form effects on urban land surface temperature and modeling seasonal correlation patterns," *Building and Environment*, 204, p. 108132. Available at: https://doi.org/10.1016/j.buildenv.2021.108132.

Liu, B. *et al.* (2024) "Urban morphology indicators and solar radiation acquisition: 2011–2022 review," *Renewable and Sustainable Energy Reviews*, 199, p. 114548. Available at: https://doi.org/10.1016/j.rser.2024.114548.

Ming, Y. *et al.* (2023) "Nonlinear effects of urban and industrial forms on surface urban heat island: Evidence from 162 Chinese prefecture-level cities," *Sustainable Cities and Society*, 89, p. 104350. Available at: https://doi.org/10.1016/j.scs.2022.104350.

Ouyang, Z. *et al.* (2022) "Albedo changes caused by future urbanization contribute to global warming," *Nature Communications*, 13(1), p. 3800. Available at: https://doi.org/10.1038/s41467-022-31558-z.

Perkins-Kirkpatrick, S. *et al.* (2024) "Extreme terrestrial heat in 2023," *Nature Reviews Earth & Environment*, 5(4), pp. 244–246. Available at: https://doi.org/10.1038/s43017-024-00536-y.

Rostami, E. and Nasrollahi, N. (2025) "The impact of urban morphology on sunlight availability at urban and neighborhood scales: A systematic review," *Sustainable Cities and Society*, 121, p. 106194. Available at: https://doi.org/10.1016/j.scs.2025.106194.

Sengupta, M. *et al.* (2018) "The National Solar Radiation Data Base (NSRDB)," *Renewable and Sustainable Energy Reviews*, 89, pp. 51–60. Available at: https://doi.org/10.1016/j.rser.2018.03.003.

Stewart, I.D. and Oke, T.R. (2012) "Local Climate Zones for Urban Temperature Studies," *Bulletin of the American Meteorological Society*, 93(12), pp. 1879–1900. Available at: https://doi.org/10.1175/BAMS-D-11-00019.1.

Tavakol, A., Rahmani, V. and Harrington, J. (2020) "Evaluation of hot temperature extremes and heat waves in the Mississippi River Basin," *Atmospheric Research*, 239, p. 104907. Available at: https://doi.org/10.1016/j.atmosres.2020.104907.

Wu, S. *et al.* (2024) "The interplay of cloud cover and 3D urban structures reduces human access to sunlight," *Nature Cities*, 1(10), pp. 686–694. Available at: https://doi.org/10.1038/s44284-024-00120-x.

Yang, J. *et al.* (2023) "Impacts of urban morphology on sensible heat flux and net radiation exchange," *Urban Climate*, 50, p. 101588. Available at: https://doi.org/10.1016/j.uclim.2023.101588.

Yu, H. *et al.* (2025) "How does urbanization process affect urban heat island effect? Interpretation of 31 cities in China based on local climate zones," *Environmental Research Letters*, 20(11), p. 114013. Available at: https://doi.org/10.1088/1748-9326/ae0da5.

Zhang, X. *et al.* (2019) "A Method Based on Temporal Component Decomposition for Estimating 1-km All-Weather Land Surface Temperature by Merging Satellite Thermal Infrared and Passive Microwave Observations," *IEEE Transactions on Geoscience and Remote Sensing*, 57(7), pp. 4670–4691. Available at: https://doi.org/10.1109/TGRS.2019.2892417.

Zhang, X. *et al.* (2021) "A practical reanalysis data and thermal infrared remote sensing data merging (RTM) method for reconstruction of a 1-km all-weather land surface temperature," *Remote Sensing of Environment*, 260, p. 112437. Available at: https://doi.org/10.1016/j.rse.2021.112437.

Zhou, J. *et al.* (2017) "A Thermal Sampling Depth Correction Method for Land Surface Temperature Estimation From Satellite Passive Microwave Observation Over Barren Land," *IEEE Transactions on Geoscience and Remote Sensing*, 55(8), pp. 4743–4756. Available at: https://doi.org/10.1109/TGRS.2017.2698828.